Accepted Manuscript

Photocatalytic activity, optical and ferroelectric properties of $Bi_{0.8}Nd_{0.2}FeO_3$ nanoparticles synthesized by sol-gel and hydrothermal methods

Hamed Maleki

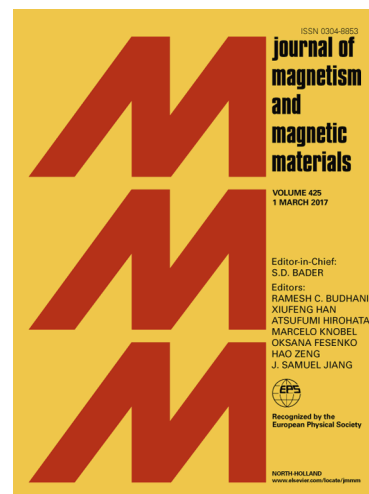Please cite this article as: H. Maleki, Photocatalytic activity, optical and ferroelectric properties of $Bi_{0.8}Nd_{0.2}FeO_3$ nanoparticles synthesized by sol-gel and hydrothermal methods, *Journal of Magnetism and Magnetic Materials* (2018), doi: https://doi.org/10.1016/j.jmmm.2018.03.043

Photocatalytic activity, optical and ferroelectric properties of $Bi_{0.8}Nd_{0.2}FeO_3$ nanoparticles synthesized by sol-gel and hydrothermal methods

Hamed Maleki[*]

Faculty of Physics, Shahid Bahonar University of Kerman, Kerman, Iran

e-mail address: hamed.maleki@uk.ac.ir

Abstract: In this study, the effects of synthesis method and dopant Neodymium ion on the ferroelectric properties and photocatalytic activity of bismuth ferrite were studied. $BiFeO_3$ (BFO) and $Bi_{0.8}Nd_{0.2}FeO_3$ (BNFO) nanoparticles were prepared through a facile sol-gel combustion (SG) and hydrothermal (HT) methods. The as-prepared products were characterized by X-ray powder diffraction (XRD), Furrier transform infrared spectroscopy (FTIR) and transmission electron microscope (TEM) images. Both nanophotocatalysts have similar crystal structures, but the SG products have semi-spherical morphology. On the other hand, HT samples have rod-like morphology. The ferroelectric properties of BNFO nanoparticles were improved compared to the undoped bismuth ferrite. The photocatalytic activity of as-synthesized nanoparticles was also evaluated by the degradation of methyl orange (MO) under visible light irradiation. The SG as-prepared nanoparticles exhibited a higher photocatalytic activity compared to powders obtained by HT method. Also substitution of Nd into the BFO structure increased the photocatalytic activity of bismuth ferrite.

1. Introduction

Multiferroic materials have simultaneously the properties of ferroelectricity, ferromagnetism and also in some cases ferroelasticity [1,2]. Data storage, sensors, spintronic devices, microwave absorption, photocatalysts and photovoltaic facilities are only some

1

application of these material [3–11]. Bismuth ferrite is the only known multiferroics that has rhombohedrally-distorted perovskite structure with the space group R_3C [4] and shows both ferroelectricity and ferromagnetism at room temperature (RT) [12,13]. $BiFeO_3$ (BFO) has the ferroelectric order below the Curie temperate $T_C \sim 1103K$ and antiferromagnetic behavior below the Neel temperature $T_N \sim 643K$ [14,15].

In recent years, BFO has received new attention due to its narrow optical band-gap (2.19 eV) and excellent chemical stability, which allows the photocatalytic activity under visible light beside other photocatalysts like TiO_2, CdS, CdSe and so on [3,16–24]. BFO shows different catalytic activities such as oxidation of organic compounds and degradation of pollutants [25–27]. In addition, BFO nanoparticles are magnetic semiconductor materials which could be separable in aqueous organic media [17]. However, there are some difficulties for different applications of BFO. Weak ferroelectricity, high leakage current density and inhomogeneous weak magnetization are some of these challenges [28–31].

Many theoretical and experimental studies have been investigated to expand the applications and solve these problems hindering practical usage of BFO. In order to improve multiferroic properties and photocatalytic activity of BFO, many modification have been investigated which includes doping rare earth elements instead of bismuth into the BFO structure [18,32–42].

In recent years, there has been many reports on preparation methods for BFO nanoparticles with a focus on photocatalytic applications, which includes sol-gel route [43,44], co-precipitation [45] and hydrothermal reaction [46–48]. However, as the morphology of nanoparticles affects the physical properties of bismuth ferrite, we are interested to study the effect of synthesis process on the photocatalytic activity of all samples, as well as other physical properties of BFO and BNFO nanoparticles. Although several researches on the structural, optical and multiferroic properties of bismuth ferrite has been done, few studies have investigated on the photocatalytic activity of Nd-doped BFO and the influence of synthesis process [49,50]. The goal of this study is to quantify the effect of Nd dopant on photocatalytic degradation rates of MO. Furthermore, BFO and BNFO were characterized for the structure, morphology, energy band-gap. Moreover thermal, ferroelectric, leakage current density and magnetic properties of samples are investigated and compared between SG and HT as-synthesized products.

2. Experimental method

2.1 Sol-gel preparation of pure and Nd-doped BiFeO$_3$

In the sol-gel method, stoichiometric amount of Bi(NO$_3$)$_3$.5H$_2$O, Fe(NO$_3$)$_3$.9H$_2$O and Nd(NO$_3$)$_3$.6H$_2$O were dissolved in deionized water separately. Meantime, ethylene glycol (EG) and 2-methoxyethanol were mixed under stirring. Then, acetic acid was added to the solution dropwise (The pH of the mixed solution was adjusted to 1.5). This solution was mixed together under vigorous stirring for 30 min. Then metal nitrate solutions were mixed with fuel solution under constant stirring. After 30 min stirring, a dark red mixture is appeared. Then, the temperature adjusted at 70 ^{o}C and after 3 hours heating and stirring, a clear brownish gel was obtained and following a few minutes with a temperature higher than 90 ^{o}C, a yellow suspension is formed. The suspension was kept at RT for 10 hours and then it was put at 115 ^{o}C for the water evaporation and fuel combustion. Finally the obtained powder was calcined at 650 ^{o}C for 5 hours before investigating the characteristics.

2.2 Hydrothermal synthesis of BFO and BNFO

In the next part, BiFeO$_3$ and Bi$_{0.8}$Nd$_{0.2}$FeO$_3$ nanoceramics were synthesized by a hydrothermal process. Typically, bismuth (III) nitrate pentahydrate, ferric (III) nitrate nonahydrate, and neodymium nitrate hexahydrate (for BNFO) were dissolved in the minimum amount of deionized water as a specified stoichiometric ratio. The mixture wad dropped into potassium hydroxide (4M, 30 ml) under magnetic stirring. After stirring for 30 min, the mixture was placed in a teflon-lined steel autoclave of 50 ml for the hydrothermal reaction with a filling capacity of 80 % and performed at 200°C for 12 hours in an oven and then cooled to RT naturally. The products are collected and washed several times with distilled water and ethanol and dried at 110 ^{o}C for 2 h before further characterization.

2.3 Characterization

The phase analysis and structural properties of BFO and BNFO nanoparticles which are synthesized via both sol-gel and hydrothermal methods, were characterized by using XRD analysis (Philips powder diffractometer) with Cu-Kα radiation (λ=1.5406 Å) and Furrier transform inferared (FTIR) TENSOR27 spectrometer. Crystal sizes also were determined by the Scherrer method. Transmission electron microscope (TEM Leo-912-AB) was performed to study the morphology and size of products. The thermal behavior of the as-prepared samples are monitored by thermogravitometric and differential thermal analysis (TG/DTA NETZSCH- PC Luxx 409) with the heating rate of 10°C/min up to 1000°C. For the magnetic properties, the hysteresis loops are recorded up to 20 KG with the vibrating sample

magnetometer (VSM- Lake Shore model 7410, SAIF) at RT. The optical properties of products were studied by UV-vis absorption spectra by using Lambda900 spectrophotometer. The polarization electric field P-E hysteresis loops of the prepared pellets were measured by the Sawyer- Tower circuit.

2.4 Photocatalytic activity measurements

The photocatalytic activity of the BFO and BNFO nanoparticles for decomposition of methyl orange (MO) was studied under irradiation of visible light source at the natural pH value. The reaction temperature was also kept at RT. The initial concentration of MO was 15 mgl^{-1} with dispersing 0.1g BFO or BNFO in 200ml aqueous solution. Before irradiation, in order to reach an adsorption equilibrium of MO on products surface, the aqueous suspension was magnetically stirred for 75 min in the dark. Then the lamp was turned on and changes of MO concentration were measured by measuring the absorbance of the solution at 554 nm using a UV-vis spectrophotometer. C/C_0, where C was the concentration of MO at time t, and C_0 was the initial concentration of MO, was the photocatalytic degradation ratio of MO which has been investigated in this study.

3. Results and discussion

3.1 X-ray diffraction investigation

Figs. 1 (a) and (b) show the powder XRD patterns of $BiFeO_3$ (x=0) and $Bi_{0.8}Nd_{0.2}FeO_3$ (x=0.2) nanoparticles prepared by SG method. Analysis of patterns indicated that all products have a single perovskite phase with distorted rhombohedral structure with the space group R_3C. All samples reveal peaks that can be assigned to the standard card of BFO perovskite structure (JCPDS card No. 86-1518). By substituting 20% neodymium, a slight shifting of peaks towards lower angles occurred and a phase transformation from rhombohedral to tetragonal structure was observed (two major peaks at $30<2\theta<33$ merged into a one peak) and intensity of peaks were decreased. The width of the BFO peaks also increased with merging the nearby peaks. The size of products was calculated by using the Scherrer formula: $D = \frac{0.89\lambda}{\beta \cos\theta}$, where λ is the wavelength of X-ray source, β is the width of the observed diffraction peak at its half intensity maximum, and θ is the Bragg angle of each peak. The obtained average nanocrystal sizes were 51 and 46 nm for BFO and BNFO respectively.
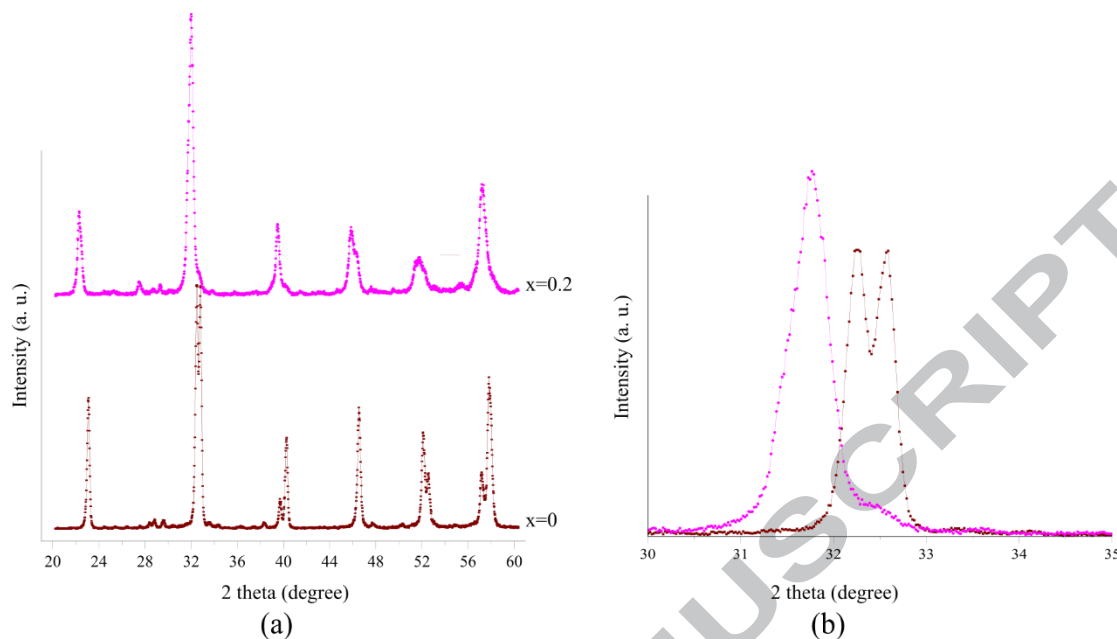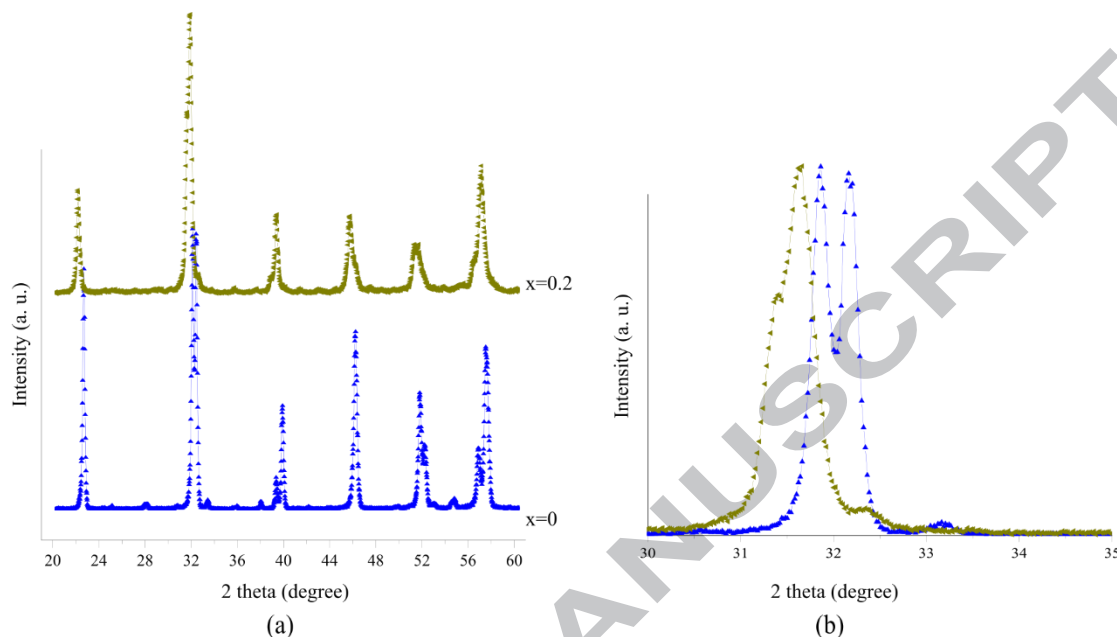
Fig. 1. (a) XRD patterns of BiFeO$_3$ and Bi$_{0.8}$Nd$_{0.2}$FeO$_3$ nanoparticles prepared by SG method. (b) Same graph in the range of 30<2θ<35

XRD patterns of as-prepared samples by HT are depicted in Fig. 2 (a) and (b). Perovskite single phase was confirmed by analysis of patterns for all nanopowders. Major peaks were index in the rhombohedral phase (R$_3$C) for BiFeO$_3$. However for the case of BNFO, two main peaks at 30<2θ<33 moved to the smaller value and furthermore, merged to form a single widened peak (Fig. 2 (b)). This behavior is due to the smaller ionic radius in Nd ions compared to Bi ions. In addition, comparison of Figs 1(b) and 2(b) indicates that width of major peacks in HT products are a little sharper compared to the as-synthesized SG samples. Finally, the analysis of particle size, pointed out that in the presence of Nd, the average size of nanoparticles decreases (~40 nm for BFO and ~36 nm for BNFO). Neither the characteristic peaks of Bi$_2$Fe$_4$O$_9$ nor of Bi$_{25}$FeO$_{40}$ were found in any of BFO and BNFO patterns.
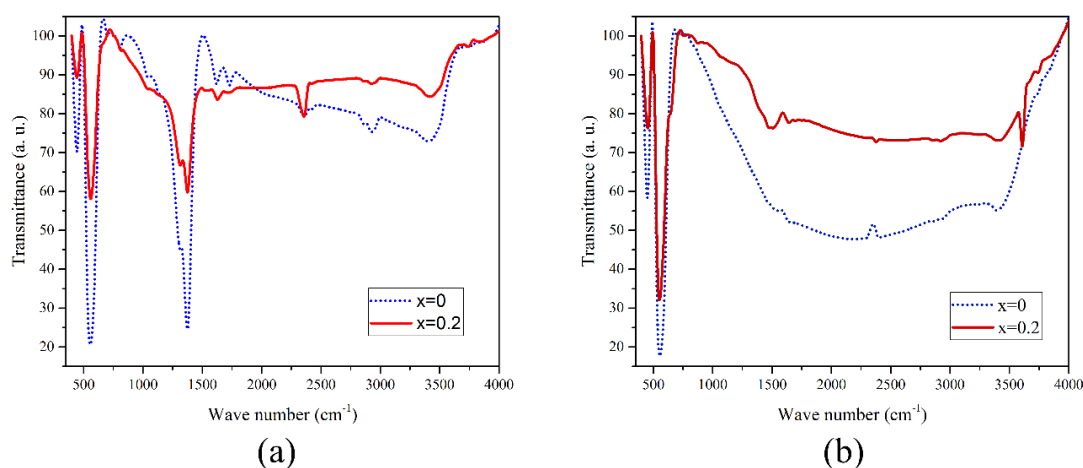
3.2 Furrier transform infrared spectroscopy

In order to further confirm the crystallinity of as-prepared products, Fig. 3 shows the FT-IR spectra of BFO and BNFO nanoparticles in the range of 400-4000 cm^{-1}. In both SG and HT cases, analysis of curves and band range 400-600 cm^{-1} is related to metal- oxygen bond and confirms the existence of perovskite structure for all samples. The vibration of Fe-O at ~450 cm^{-1} and stretching vibration of O-Fe-O bonds at ~550 cm^{-1} present in the octahedral FeO$_6$ group and in the framework can be observed below 600 cm^{-1}[51]. The broad band at 3200-3600 cm^{-1} is due to antisymmetric and symmetric stretching of H$_2$O and O-H bond

groups [52]. A strong band at around 1380 cm^{-1} was due to the presence of trapped nitrates [53].

Fig. 2. (a) X-ray diffraction plots of pure and Nd-doped bismuth ferrite nanoparticles synthesized by HT method. (b) Same patterns in the range of 30<2θ<35.

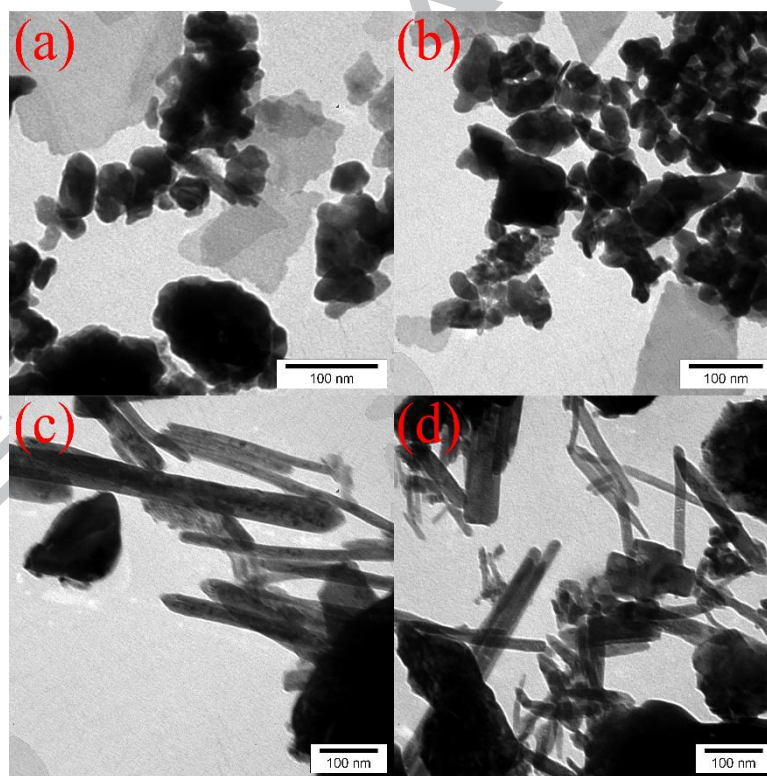**Fig. 3.** (a) FTIR spectra of BFO and BNFO nanoparticles synthesized by SG and (b) synthesized by HT method.

3.3 Transmission electron microscope

Transmission electron microscope (TEM) is used for the observation of morphology and particle distribution and size of BFO and BNFO nanoparticles. As shown in Fig. 4, all samples consisted of nano-scale particles, however the morphology of powders depending on

the synthesis method is very different. Although nanoparticles which were synthesized by SG are semi-spherical, products obtained via HT are nanorods. Figs. 4 (a) and (b) are BFO and BNFO nanoparticles that were prepared by SG method. Particles in both images are semi-spheroid and rectangular particles with some irregular shape particles which look denser. In contrast, products which were obtained from HT method have rod-like shape and look looser (Figs. 4 (c) and (d)). After incorporating the $BiFeO_3$ with Nd, it can be seen that there is no significant change in the morphology of both SG and HT products. The size of nanoparticles obtained from TEM is a little larger than that obtained from the Scherrer equation. According to analysis of images, the average size of SG as-prepared products were obtained 55 and 51 nm for BFO and BNFO nanoparticles and a thickness length ranging from 45-50 nm and 39-42 nm for HT as-prepared BFO and BNFO powders. The length of nanorods was also in a range of 80-300 nm. The results demonstrate a clear influence of the preparation method on the structural features of the prepared nanocomposites.

Fig. 4. (a) and (b) TEM images of $BiFeO_3$ and $Bi_{0.8}Nd_{0.2}FeO_3$ synthesized by SG method. (c) and (d) show BFO and BNFO nanopowders prepared via HT route.
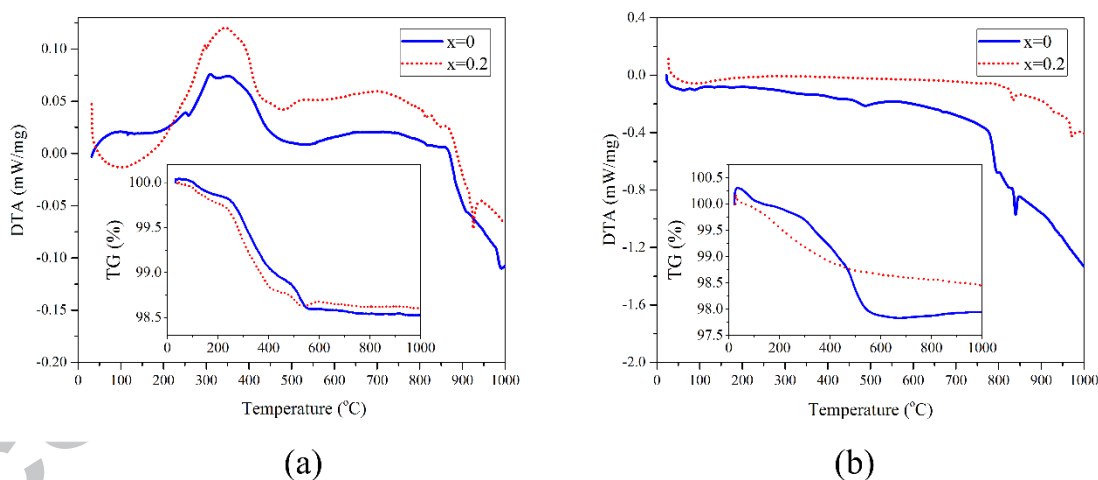
3.4 Thermal behavior

Fig. 5 (a) shows the differential thermal analysis (DTA) curves of BFO and BNFO nanograins synthesized by SG. The inset also indicates the thermogravimetric (TG) analysis

of samples. From RT up to 180 °C, for BFO nanoparticles, an exothermic peak can be seen with an instance of 0.2% reduction in weight. This peak can be attributed to hydrate thermal and the nitrate present in the course of evaporation as well as evaporating water on nanoparticle's surface. In the range of 400-600°C, one can observe a small exothermic peak as well as a weight reduction of 0.15%. This peak is an indication of the oxidation reaction between Fe^{3+} and Bi^{3+} and it is considered as an evidence for the crystal phase of BFO [9]. In the range of 820-840 °C, an endothermic peak appears which is due to electrical transmission temperature (T_C ~ 830 ^{o}C). For $Bi_{0.8}Nd_{0.2}FeO_3$ in DTA curve, decomposition of hydrate and nitrate peaks were eliminated and the weight was declined up to 0.15%. Also, in the lower temperature (T_C ~828 ^{o}C) the ferroelectric phase transition occurred (exothermic peak).

Inset in Fig. 5 (a) shows thermal gravitometric analysis (TGA) of all as-prepared nanopoders. In the curves, up to 200°C the loss of physisorbed water is observed. The second part (200-450°C) corresponds to the loss of surface hydroxyl groups. Finally the decomposition of starting spices is occurred in the weight loss above 500°C [52].

Fig. 5. (a) DTA and TG (as an inset) curves of BFO and BNFO nanoparticles synthesized by sol-gel method. (b) Same curves for as-prepared BFO and BNFO nanoparticles synthesized by hydrothermal method.

Same as Fig. 5 (a), in Fig.5 (b) differential thermal analysis curves of $BiFeO_3$ and $Bi_{0.8}Nd_{0.2}FeO_3$ nanocrystals are shown. These substances are synthesized by hydrothermal method. In DTA curves for a temperature at the range up to 200°C, an exothermic peak can be observed. This peak is due to available nitrate and evaporating water on the surface of nanoparticles. In the range of 400-600°C a small exothermic peak is seen. This peak indicates

the oxidation reaction between Fe^{3+} and Bi^{3+}. This can confirm the existence of crystal phase for BFO and 20%Nd-doped BFO. A phase transition at 833 ^{o}C for $BiFeO_3$ and 831 ^{o}C for $Bi_{0.8}Nd_{0.2}FeO_3$ can be seen in the measurements, which is related to the Curie temperature.

3.5 M-H hysteresis loops analysis of BFO and BNFO

The RT magnetic hysteresis loops for all samples are shown in Fig. 6. In contrast to the magnetic behavior of bulk bismuth ferrite (antiferromagnetism), all as-synthesized nanoparticles showed weak ferromagnetism in agreement with other reports [13,54,55]. All information of magnetic characterization for BFO and BNFO nanoparticles that synthesized via SG and HT methods listed in Table 1. According to literature, in $BiFeO_3$ the magnetization and magnetic properties, related to the iron ions (Fe^{3+}). Each iron ion was surrounded with six other ions with nonparallel spins. These spins are organized in a spiral manner with a period of 62nm, which leads to a magnetization value zero. When the particle size is reduced to less than 62 nm, this spiral manner is broken and weak ferromagnetism is occurred [5,13]. When 20%Nd enters into the structure of BFO, saturated magnetization (M_s) decreases. However, coercive force (H_c) increases. The remanent magnetization in HT-prepared samples is also increased, but for the SG-prepared samples, M_r decreased. Furthermore, by adding neodymium, the size of nanoparticles has declined.

Fig. 6. (a) RT Magnetization- applied magnetic field (M-H) hysteresis loops of $BiFeO_3$ and $Bi_{0.8}Nd_{0.2}FeO_3$ nanopowders synthesized by SG method. (b) Same curves for as-prepared BFO and BNFO nanoparticles synthesized through HT.

For the HT-prepared samples, loops are not saturated up to 20 KG. This can be interpreted trough the existence of both ferromagnetic and antiferromagnetic orders inside the

9

HT-synthesized nanorods. The saturated magnetization in SG-prepared samples is much higher compare to the other ones. On the other hand, the coercive force for samples obtained from HT method, is slightly higher than the SG prepared samples. The reason can be explained due to the morphology of nanoparticles which are completely different according to synthesis methods.
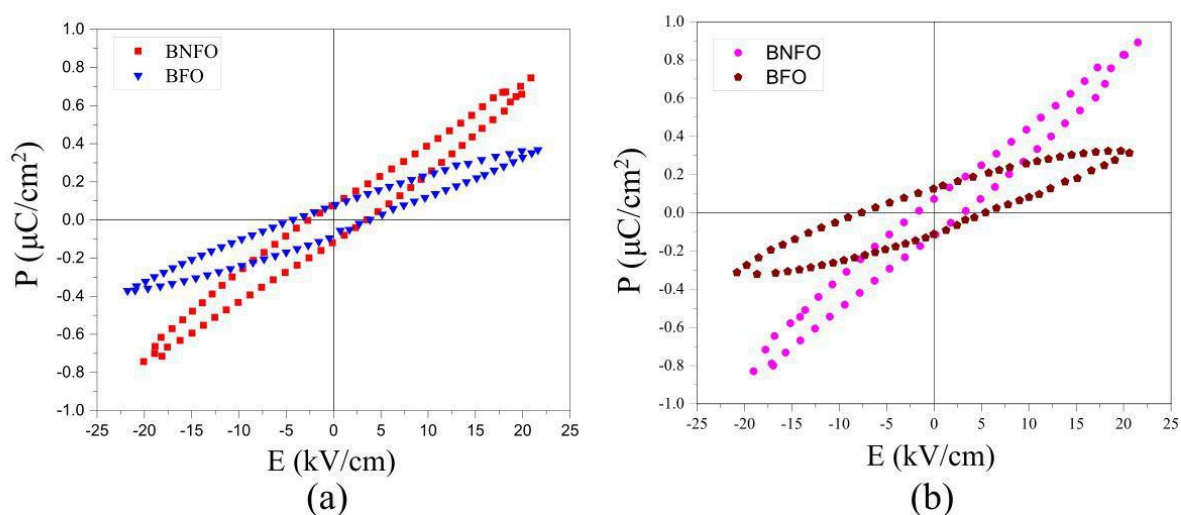
Table 1. Information from magnetic characterization for BFO and BNFO synthesized by sol gel and hydrothermal

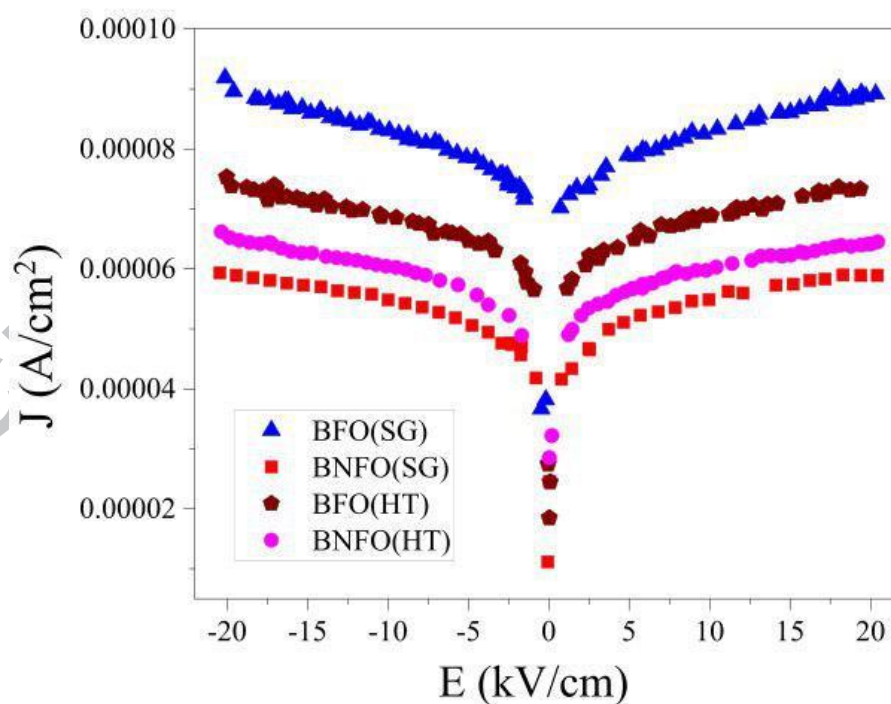| Sample	Sol gel			Hydrothermal		
	M_s(emu/g)	M_r(emu/g)	H_c(G)	M_s(emu/g)	M_r(emu/g)	H_c(G)
$BiFeO_3$	0.63	0.0027	63.28	0.1093	0.0074	208.97
$Bi_{0.8}Nd_{0.2}FeO_3$	0.54	0.0068	167.90	0.0096	0.0037	332.69

3.6 Ferroelectric properties of $BiFeO_3$ and $Bi_{0.8}Nd_{0.2}FeO_3$ nanoceramics

In order to study the ferroelectric properties of products, here, the as-synthesized BFO and BNFO nanoparticles were pressed and were coated with a thin layer (~30 nm) of silver as electrodes by using DC sputtering. Fig. 7 presents the RT polarization-electric field (P-E) hysteresis loops of BFO and BNFO nanoparticles synthesis by SG and HT methods under applied electric field up to 25 kV/cm. It can be seen that for all products loops are unsaturated. By adding Nd, into the structure of BFO, the saturated polarization is increased. However in both synthesis method results, remanent polarization and coercive field are decreased and reduced the leakage current [56,57]. The reduction of leakage current by doping Nd, is due to a reduction of oxygen vacancies [58,59]. When Nd is doped to BFO, the P-E loop is improved showing an elongated loop compared to the BFO samples.

In order to study the influence of Nd on the ferroelectric behavior of all products, leakage current density- electric field (J-E) curves of $BiFeO_3$ and $Bi_{0.8}Nd_{0.2}FeO_3$ nanoparticles synthesized by SG and HT at RT is plotted in Fig. 8. BFO (BNFO) nanoparticles synthesized via SG show high leakage current compared to the BFO nanorods which were synthesized by HT. Although the J is decreased with the dopant Nd in the nanoparticles and remained much lower than that of BFO, the synthesis method also affects the leakage current and in the case of BNFO, the products synthesized by HT route shows the bigger leakage current density.
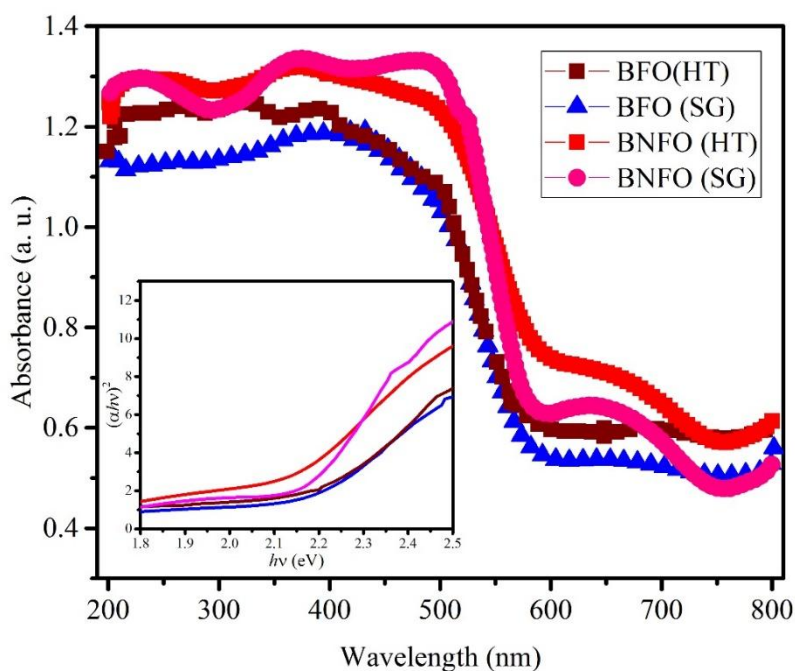
Fig. 7. P-E hysteresis loops of BFO and BNFO nanoparticles synthesized by (a) sol-gel and (b) hydrothermal.

Fig. 8. RT current density- applied electric field (J-E) BFO and BNFO nanoparticles synthesized by SG and HT.
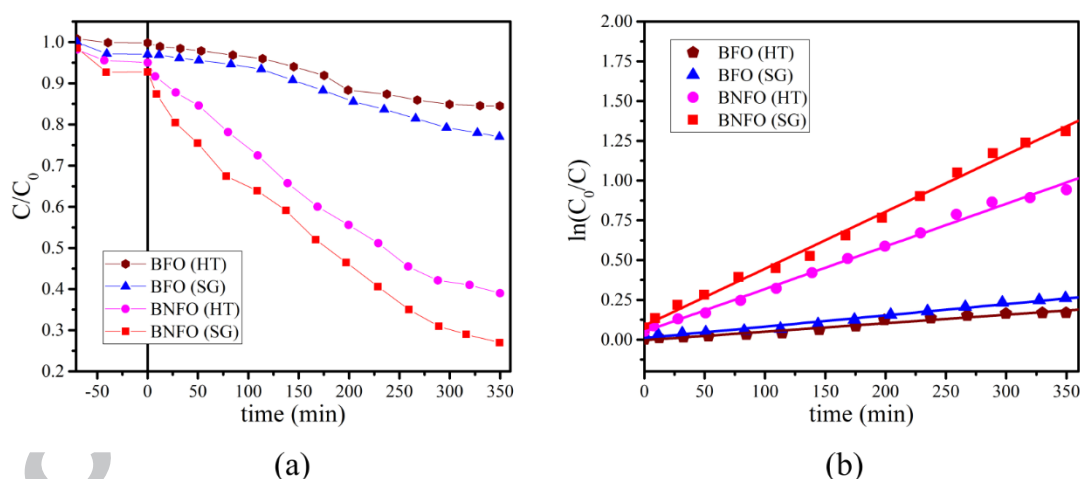
11

3.7 Uv-vis spectroscopy analysis

The optical band-gap of BiFeO$_3$ and Bi$_{0.8}$Nd$_{0.2}$FeO$_3$ nanoparticles have been calculated with the help of absorbance spectra. Fig. 9 shows the UV-vis absorption spectra of all products. By using Tauc's equation, the energy band-gap (E$_g$), absorption coefficient (α), is related by (for materials with direct band-gap): $(\alpha h\nu)^2 = K(h\nu - E_g)$, where *K* is a constant and hν is the photon energy. An inset in Fig.8 indicates the plot of $(\alpha h\nu)^2$ vs hν for BiFeO$_3$ and Bi$_{0.8}$Nd$_{0.2}$FeO$_3$ nanoparticles synthesis by SG and HT methods. The extrapolated straight line fitted to the linear part of curves gives the value of E$_g$. The extracted values of E$_g$ for BFO (BNFO) nanoparticles synthesis by SG method is ~ 2.13 eV (2.08 eV) and 2.11 eV (2.04 eV) for products that obtained from HT reaction route. Slight decrease of E$_g$ value by Nd doping was observed which indicates the narrowing of the optical band-gap and enhanced photocatalytic activity and photovoltaic effects.

Fig. 9. UV-vis spectrum of BiFeO$_3$ and Bi$_{0.8}$Nd$_{0.2}$FeO$_3$ nanoceramics prepared by SG and HT methods. Inset shows $(\alpha h\nu)^2$ versus *hv* plots of all samples.

3.8 Photocatalytic activity of BFO and BNFO

The photocatalytic activity of products were evaluated by degrading methyl orange (MO) in an aqueous solution under visible light irradiation. The reaction rate constant of samples are plotted in Fig. 10. The first-order rate constant is calculated by the equation $\ln(C_0/C) = \kappa t$, where C_0 and C are concentrations of MO in solution at the beginning and at time t. The reaction rate constant (κ) is defined as a slope in the apparent of $\ln(C_0/C)$ versus time. All BFO and BNFO nanoparticles have visible light induced photocatalytic activity. Nanocatalysts synthesized by SG (polyhedral morphology) shows better photocatalytic activity compared to hydrothermal prepared samples (rod-like). This can be explained due to the morphology, crystallite size and surface area of powders. The SG-synthesized (HT-synthesized) BFO nanoparticles showed ~ 23% (16%) degradation of MO in 350 min. Remarkably, the 20%Nd-substitution has a significant effect on the photocatalytic activity of BiFeO$_3$. The total removal of MO by SG-synthesized (HT-synthesized) BNFO is 73% (61%).

Fig. 10. (a) Photocatalytic degradation rates of BFO and BNFO nanoparticles prepared by SG and HT methods under visible light irradiation. (b) Represents the pseudo-first-order kinetics curves of the MO degradation.

4. Conclusions

In this work the influence of synthesis method, as well as addition of 20%Nd into the structure of bismuth ferrite on the multiferroic properties and photocatalytic activity of BiFeO$_3$ and Bi$_{0.8}$Nd$_{0.2}$FeO$_3$ nanoparticles was investigated by different characterization methods. In all Nd-doped samples, the location of main peaks changes slightly due to Nd doping and the two main peaks around $2\theta \sim 32^\circ$ merged into a one wide peak, with is

correspond to the structural phase transformation from rhombohedral to tetragonal structure. DTA measurements indicated that by addition of Nd, the Curie temperature is decreased. Magnetic properties of all as-prepares samples were depended strongly to the synthesis method which is related to the morphology and particle size of nanoparticles. Furthermore, by addition of neodymium, the saturation magnetization was decreased. The ferroelectric properties of pure and Nd-doped BFO indicated that the Nd-substitution, enhanced the ferroelectric characteristics of samples and reduced the leakage current. Finally photocatalytic degradation of methylene orange (MO) under visible light irradiation was implemented. The results indicated that the photocatalytic activity of nanoceramics depends not only on the synthesis method but also on the addition Nd into the structure of bismuth ferrite.

5. References

[1]   Y. Tokura, S. Seki, N. Nagaosa, Reports on Progress in Physics 77(7) (2014) 76501.

[2]   L.W. Martin, S.P. Crane, Y.-H. Chu, M.B. Holcomb, M. Gajek, M. Huijben, C.-H. Yang, N. Balke, R. Ramesh, Journal of Physics: Condensed Matter 20(43) (2008) 434220.

[3]   J. Wang, J.B. Neaton, H. Zheng, V. Nagarajan, S.B. Ogale, B. Liu, D. Viehland, V. Vaithyanathan, D.G. Schlom, U. V Waghmare, N.A. Spaldin, K.M. Rabe, M. Wuttig, R. Ramesh, Science (New York, N.Y.) 299(5613) (2003) 1719.

[4]   W. Eerenstein, N.D. Mathur, J.F. Scott, Nature 442(7104) (2006) 759.

[5]   J. Wang, J.B. Neaton, H. Zheng, V. Nagarajan, S.B. Ogale, B. Liu, D. Viehland, V. Vaithyanathan, D.G. Schlom, U. V Waghmare, N.A. Spaldin, K.M. Rabe, M. Wuttig, R. Ramesh, Science (New York, N.Y.) 299(5613) (2003) 1719.

[6]   H.T. Yi, T. Choi, S.G. Choi, Y.S. Oh, S.-W. Cheong, Advanced Materials 23(30) (2011) 3403.

[7]   W. Ji, K. Yao, Y.C. Liang, Advanced Materials 22(15) (2010) 1763.

[8]   S.Y. Yang, L.W. Martin, S.J. Byrnes, T.E. Conry, S.R. Basu, D. Paran, L. Reichertz, J. Ihlefeld, C. Adamo, A. Melville, Y.-H. Chu, C.-H. Yang, J.L. Musfeldt, D.G. Schlom, J.W. Ager, R. Ramesh, Applied Physics Letters 95(6) (2009) 62909.

14

[9]   D. Wang, M. Wang, F. Liu, Y. Cui, Q. Zhao, H. Sun, H. Jin, M. Cao, Ceramics
       International 41(7) (2015) 8768.

[10]   Y. Li, M. Cao, Materials & Design 110 (2016) 99.

[11]   Y. Li, X. Fang, M. Cao, Scientific Reports 6(1) (2016) 24837.

[12]   N. Hur, S. Park, P.A. Sharma, J.S. Ahn, S. Guha, S.-W. Cheong, Nature 429(6990)
       (2004) 392.

[13]   G. Catalan, J.F. Scott, Advanced Materials 21(24) (2009) 2463.

[14]   C. Tabares-Muñoz, J.-P. Rivera, A. Bezinges, A. Monnier, H. Schmid, Japanese
       Journal of Applied Physics 24(S2) (1985) 1051.

[15]   P. Fischer, M. Polomska, I. Sosnowska, M. Szymanski, Journal of Physics C: Solid
       State Physics 13(10) (1980) 1931.

[16]   F. Gao, X.Y. Chen, K.B. Yin, S. Dong, Z.F. Ren, F. Yuan, T. Yu, Z.G. Zou, J.-M. Liu,
       Advanced Materials 19(19) (2007) 2889.

[17]   S. Li, Y.-H. Lin, B.-P. Zhang, Y. Wang, C.-W. Nan, The Journal of Physical
       Chemistry C 114(7) (2010) 2903.

[18]   R. Guo, L. Fang, W. Dong, F. Zheng, M. Shen, The Journal of Physical Chemistry C
       114(49) (2010) 21390.

[19]   Y. Huo, Y. Jin, Y. Zhang, Journal of Molecular Catalysis A: Chemical 331(1–2)
       (2010) 15.

[20]   X. Wang, W. Mao, J. Zhang, Y. Han, C. Quan, Q. Zhang, T. Yang, J. Yang, X. Li, W.
       Huang, Journal of Colloid and Interface Science 448 (2015) 17.

[21]   T. Gao, Z. Chen, Y. Zhu, F. Niu, Q. Huang, L. Qin, X. Sun, Y. Huang, Materials
       Research Bulletin 59 (2014) 6.

[22]   M. Ni, M.K.H. Leung, D.Y.C. Leung, K. Sumathy, Renewable and Sustainable Energy
       Reviews 11(3) (2007) 401.

[23]   Q. Li, B. Guo, J. Yu, J. Ran, B. Zhang, H. Yan, J.R. Gong, Journal of the American
       Chemical Society 133(28) (2011) 10878.

[24]   Y. Chen, L. Wang, W. Wang, M. Cao, Applied Catalysis B: Environmental 209 (2017)

110.

[25] T. Soltani, M.H. Entezari, Journal of Molecular Catalysis A: Chemical 377 (2013) 197.

[26] Z. Li, Y. Shen, Y. Guan, Y. Hu, Y. Lin, C.-W. Nan, J. Mater. Chem. A 2(6) (2014) 1967.

[27] S. Sun, W. Wang, L. Zhang, M. Shang, The Journal of Physical Chemistry C 113(29) (2009) 12826.

[28] H. Singh, K.L. Yadav, Journal of Physics: Condensed Matter 23(38) (2011) 385901.

[29] X. Qi, J. Dho, R. Tomov, M.G. Blamire, J.L. MacManus-Driscoll, Applied Physics Letters 86(6) (2005) 62903.

[30] H. Maleki, S. Falahatnezhad, M. Taraz, Journal of Superconductivity and Novel Magnetism (2018) 1.

[31] H. Maleki, M. Haselpour, R. Fathi, Journal of Materials Science: Materials in Electronics 29(5) (2018) 4320.

[32] D.H. Wang, W.C. Goh, M. Ning, C.K. Ong, Applied Physics Letters 88(21) (2006) 212907.

[33] Y.-H. Lee, J.-M. Wu, C.-H. Lai, Applied Physics Letters 88(4) (2006) 42903.

[34] S. Karimi, I.M. Reaney, Y. Han, J. Pokorny, I. Sterianou, Journal of Materials Science 44(19) (2009) 5102.

[35] R.K. Mishra, D.K. Pradhan, R.N.P. Choudhary, A. Banerjee, Journal of Magnetism and Magnetic Materials 320(21) (2008) 2602.

[36] F. Huang, X. Lu, W. Lin, X. Wu, Y. Kan, J. Zhu, Applied Physics Letters 89(24) (2006) 242914.

[37] T. Soltani, B.-K. Lee, Journal of Hazardous Materials 316 (2016) 122.

[38] Y.-L. Pei, C. Zhang, Journal of Alloys and Compounds 570 (2013) 57.

[39] S. Mohammadi, H. Shokrollahi, M.H. Basiri, Journal of Magnetism and Magnetic Materials 375 (2015) 38.

[40] D.O. Alikin, A.P. Turygin, J. Walker, A. Bencan, B. Malic, T. Rojac, V.Y. Shur, A.L.

Kholkin, Acta Materialia 125 (2017) 265.

[41]   H. Maleki, S. Zare, R. Fathi, Journal of Superconductivity and Novel Magnetism (2017) 1.

[42]   J. Reszczyńska, T. Grzyb, Z. Wei, M. Klein, E. Kowalska, B. Ohtani, A. Zaleska-Medynska, Applied Catalysis B: Environmental 181 (2016) 825.

[43]   Z. Hu, D. Chen, S. Wang, N. Zhang, L. Qin, Y. Huang, Materials Science and Engineering: B 220 (2017) 1.

[44]   G. Arya, J. Yogiraj, N.S. Negi, J. Shah, R.K. Kotnala, Journal of Alloys and Compounds 723 (2017) 983.

[45]   Z. Liu, Y. Qi, C. Lu, Journal of Materials Science: Materials in Electronics 21(4) (2010) 380.

[46]   C.C. Chen, T. Fan, Journal of Materials Science: Materials in Electronics 28(14) (2017) 10019.

[47]   T. Gao, Z. Chen, F. Niu, D. Zhou, Q. Huang, Y. Zhu, L. Qin, X. Sun, Y. Huang, Journal of Alloys and Compounds 648 (2015) 564.

[48]   X. Wang, W. Mao, Q. Zhang, Q. Wang, Y. Zhu, J. Zhang, T. Yang, J. Yang, X. Li, W. Huang, Journal of Alloys and Compounds 677 (2016) 288.

[49]   R. Dhanalakshmi, P. Reddy Vanga, M. Ashok, N. V. Giridharan, IEEE Magnetics Letters 7 (2016) 1.

[50]   Z. Chen, Y. Wu, X. Wang, W. Jin, C. Zhu, Journal of Materials Science: Materials in Electronics 26(12) (2015) 9929.

[51]   T. Liu, Y. Xu, S. Feng, J. Zhao, Journal of the American Ceramic Society 94(9) (2011) 3060.

[52]   G. Biasotto, A. Simões, C. Foschini, S. Antônio, M. Zaghete, J. Varela, Processing and Application of Ceramics 5(3) (2011) 171.

[53]   A. V. Zalesskii, A.A. Frolov, T.A. Khimich, A.A. Bush, Physics of the Solid State 45(1) (2003) 141.

[54]   † Tae-Jin Park, ‡ Georgia C. Papaefthymiou, ‡ Arthur J. Viescas, § and Arnold R.

Moodenbaugh, †,§ Stanislaus S. Wong*, (2007).

[55]   W. Hu, Y. Chen, H. Yuan, G. Li, Y. Qiao, Y. Qin, S. Feng, The Journal of Physical Chemistry C 115(18) (2011) 8869.

[56]   S.K. Pradhan, J. Das, P.P. Rout, V.R. Mohanta, S.K. Das, S. Samantray, D.R. Sahu, J.L. Huang, S. Verma, B.K. Roul, Journal of Physics and Chemistry of Solids 71(11) (2010) 1557.

[57]   M.H. Basiri, H. Shokrollahi, G. Isapour, Journal of Magnetism and Magnetic Materials 354 (2014) 184.

[58]   G.L. Yuan, S.W. Or, J.M. Liu, Z.G. Liu, Applied Physics Letters 89(5) (2006) 52905.

[59]   P. Sharma, V. Verma, Journal of Magnetism and Magnetic Materials 374 (2015) 18.

Highlights:

- $BiFeO_3$ and $Bi_{0.8}Nd_{0.2}FeO_3$ nanoparticles were prepared by a sol-gel and hydrothermal methods.

- The prepared samples were well characterized by XRD, TEM, FTIR, TG/DTA, UV-vis and VSM.

- Effect of synthesis method, as well as the influence of 20%Nd-doping on the multiferroic properties and photocatalytic activity of bismuth ferrite was investigated.

- Improved magnetic properties due to the sol-gel synthesis method.

- Improved photocatalytic activity and ferroelectric properties due to dopant neodymium.